DOI 10.1007/978-3-319-04397-5_17
Reprinted from *International Journal of Fracture*, DOI 10.1007/s10704-013-9883-7

ORIGINAL PAPER

Crack nucleation from a notch in a ductile material under shear dominant loading

A. Ghahremaninezhad · K. Ravi-Chandar

Received: 28 April 2013 / Accepted: 16 September 2013 / Published online: 16 October 2013

Abstract We examine the *nucleation* of a crack from a notch under a dominant shear loading in Al 6061-T6. The specimen is loaded in nominally pure shear over the gage section in an Arcan specimen configuration. The evolution of deformation is monitored using optical and scanning electron microscopy. Quantitative measurements of strain are made using the 2nd phase particles as Lagrangian markers which enable identification of the true (logarithmic) strains to levels in the range of two. Electron microscopy reveals further that the 2nd phase particles do not act as nucleation sites for damage in the regions of pure shear deformation. The initial notch is shown to "straighten out", forming a new, sharper notch and triggering failure at the newly formed notch. Numerical simulations of the experiment, using the conventional Johnson–Cook model and a modified version based on grain level calibration of the failure strains, reveal that it is necessary to account for large local strain levels prior to the nucleation of a crack in order to capture the large deformations observed in the experiment.

A. Ghahremaninezhad · K. Ravi-Chandar (✉)
Center for Mechanics of Solids, Structures and Materials,
The University of Texas at Austin, Austin,
TX 78712-0235, USA
e-mail:fracture@mail.ae.utexas.edu

Present affiliation:
A. Ghahremaninezhad
Department of Civil, Architectural,
and Environmental Engineering, University of Miami,
Coral Gables, FL 33146, USA

Keywords Fracture · Damage · Voids · Grain-level strain measurement

1 Introduction

The problem of ductile failure under shear has been addressed in numerous studies in the literature. Through the early investigations of Orowan (1948), Tipper (1949), Rogers (1960), Puttick (1960), and others, it is now established that failure occurs initially as a concentration of shear localization, followed by the nucleation of a large number of voids within this shear zone and their eventual coalescence. However, such failures were typically examined and observed in specimens with a triaxiality value—the ratio of the mean stress to the equivalent—in the range of 0.5–1. For pure shear loading, it is not evident how eventual failure occurs; the inability to trigger the localization that precedes failure under pure shear (low triaxiality) is rather well-known. Recently, Bao and Wierzbicki (2004), Barsoum and Faleskog (2007), Beese et al. (2010), and others have investigated failure of structural materials under conditions of high shear and low triaxiality. While the earlier results of Hancock and Mackenzie (1976) and Johnson and Cook (1985) reported a monotonic increase in the strain-to-fracture with decreasing triaxiality, the results of Beese et al. (2010) and Barsoum and Faleskog (2007) indicate a nonmonotonic dependence, with a cusp at different triaxiality levels for different materials and a drop in the strain-to-failure at lower triaxialities.

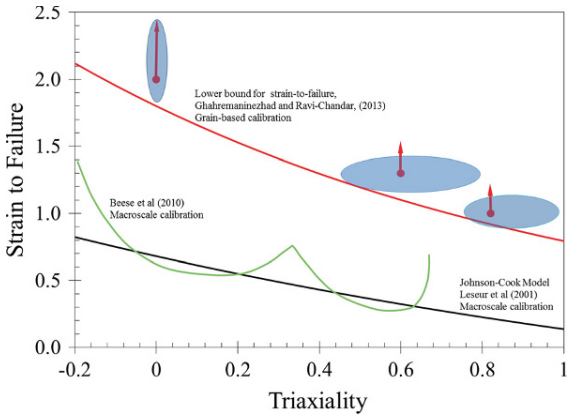

Fig. 1 Variation of strain-to-failure with triaxiality. The *blue* ellipses indicate the range of strain levels obtained from grain level measurements without damage at the levels of triaxiality indicated. Based on these, a lower bound estimate for the failure strain is suggested by the *red line*

In recent papers, (Ghahremaninezhad and Ravi-Chandar 2012, 2013; Haltom et al. 2013), we explored the appearance of very large deformations at the level of grains without development of damage in the form of voids in Al 6061-T6 alloy. Nevertheless, we reported that the final failure surface had a dimpled appearance and hence must have formed through the nucleation, growth and coalescence of voids in a localized manner. Based on these observations and measurements, a lower-bound strain-to-failure criterion that has an exponential dependence on the triaxiality as predicted by the cavity growth model of Rice and Tracey (1969) was proposed for this material, as shown in Fig. 1. The lower bound estimate of the strain-to-failure was fitted with an exponential of the form $\varepsilon_f = D_2 \exp(D_3 \sigma_m/\sigma_e)$, where σ_m is the mean stress and σ_e is the effective stress; the parameters of the model for Al 6061-T6 were found through a simple fitting procedure: $D_2 = 1.8$ and $D_3 = -0.82$. In contrast, the calibration by Lesuer et al. (2001), of the Johnson–Cook (JC) model $\varepsilon_f = D_1 + D_2 \exp(D_3 \sigma_m/\sigma_e)$ based on macroscopic strain measurements yielded the following parameters: $D_1 = -0.77$, $D_2 = 1.45$ and $D_3 = -0.47$; this failure curve is also plotted in Fig. 1. The calibration of the modified Mohr–Coulomb criterion of Beese et al. (2010) for the same Al 6061-T6 alloy is also shown in Fig. 1 for comparison. It is clear that the estimate of the lower bound for the strain-to-failure provided by Ghahremaninezhad and Ravi-Chandar (2013) is significantly higher than the traditional JC model and the modified Mohr–Coulomb model; however, it should be noted that the lower bound can be used appropriately only when the length scales at which this criterion is used are on the order of the grain size.

In this article, our main objective is to examine the predictive ability of the proposed grain level failure criterion. We accomplish this through an example dealing with crack nucleation from a notched specimen under dominant shear loading. Specifically, we consider an Arcan specimen with a notch machined by electric discharge machining to have a notch angle of $\sim 90°$ and a notch radius of $\sim 160\mu$m, subject it to a pure shear loading in the Arcan fixture, and follow the development of deformation and failure in the notch region as well as in the interior through interrupted tests. There is a body of literature that deals with a similar problem, where mixed-mode fracture initiation in specimen configurations that are dominated by the stress concentration associated with a single crack is considered. For example, Aoki et al. (1990), explored ductile failure under mixed mode loading in Al 5083-O aluminum alloy; mixed mode loading was applied in a compact-tension-shear configuration to explore crack initiation from a fatigue pre-crack. They found that one region of the pre-crack blunted, while the other region sharpened; the extent of such blunting was characterized by measuring the zone in which stretching occurred and shown to depend on the degree of mode mixity; furthermore, crack initiation was reported from the blunted crack tip since the triaxiality was higher in this region. Ghosal and Narasimhan (1994, 1996) performed finite element studies of crack response under mixed mode loading using a Gurson model that incorporates material damage, and examined various aspects of the problem, such as the debonding of inclusions, the deformation and sharpening of the notch, and the dependence of the fracture toughness on the mode mixity. They also report the separation of the pre-crack into blunted and sharpened corners, with significant void growth occurring in the blunted region. The goal of the studies cited above and others was mainly to investigate the dependence of the fracture toughness, characterized in terms of the J-integral, on mode-mixity. In contrast, the present paper is concerned with examining the evolution of deformation and the initiation of failure in specimens without an initial crack; we examine the development of deformation and damage in Al 6061-T6 leading up to the nucleation of a crack from a notch under shear dominant loading. In particular, we are interested (i) in

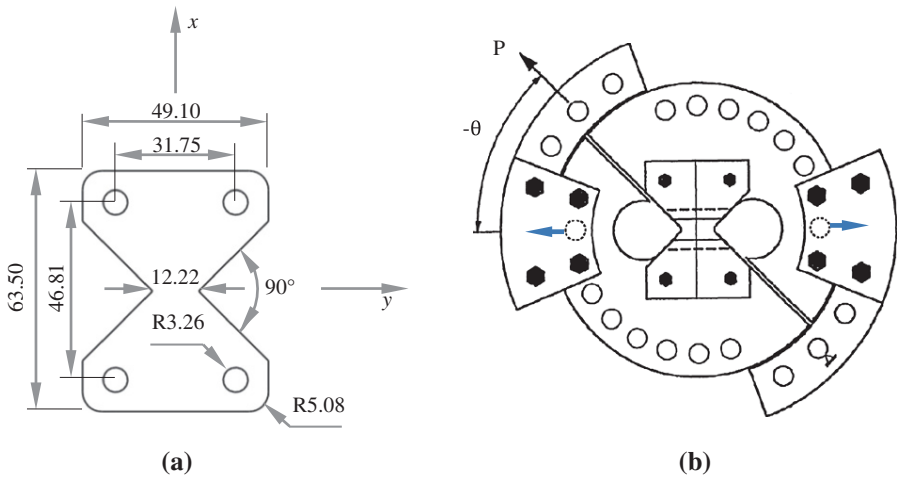

Fig. 2 **a** Geometry of the Arcan specimen (all dimensions are in mm). Rolling direction is along the x-direction. **b** Geometry of the fixture used in the modified Arcan tests (reproduced from Hung and Liechti 1999). The two *arrows* from the *dotted circles* indicate pure shear loading; other pairs of holes result in shear plus compression or tension

understanding the role of the second phase particles in generating damage, (ii) in determining how cracks are nucleated from the notch and (iii) finally in examining the use of the failure criterion presented in Ghahremaninezhad and Ravi-Chandar (2013), to simulate the nucleation of a crack.

This paper is organized as follows: experiments under pure shear loading of a notched Arcan-type specimen are described in Sect. 2. These experiments provide macroscopic measurements of the load-elongation response along with grain level strain measurements in order to provide local strain estimates. The nucleation/onset of crack initiation is also examined in this section through optical and scanning electron microscopy of interrupted tests. The response of the notched specimen is modeled in Sect. 3 using the finite element code ABAQUS, endowed with a JC model as calibrated by Lesuer et al. (2001) and also modified with the results of Ghahremaninezhad and Ravi-Chandar (2013). The main conclusions are summarized in Sect. 4.

2 Experimental results

The Arcan specimens were cut from the same rolled sheet stock (2.44 mm thick) used for the tension and shear tests described in Ghahremaninezhad and Ravi-Chandar (2012, 2013), with the rolling direction oriented along the x-direction as indicated in Fig. 2a. These specimens were loaded in a modified Arcan fixture shown in Fig. 2b. The grains are platelets that are about 14 μm thick, 46 μm wide, and 39 μm long, as characterized by Ghahremaninezhad and Ravi-Chandar (2012). In an effort to examine the grain level strains during the deformation stages, without the post-test measurements reported in our prior investigations, the specimen was polished and etched *prior to testing* using Weck's etchant (details of the specimen preparation for metallographic observations are given in Ghahremaninezhad and Ravi-Chandar 2012). The nominal stress (force/initial gage cross-sectional area) versus normalized crosshead displacement[1] response curves from one pure shear test is shown in Fig. 3. Note that the beginning of the load drop in the experiment corresponds to initiation of a crack from the notch regions and that the material continues to exhibit a strain hardening response. In order to examine the evolution of deformation and failure at the grain level, the loading on this specimen was interrupted at different stages along the overall response at points indicated as A, B, and C and then taken to final failure at D; at each of these stages, optical micrographs of the x–y plane near the center of the specimen were taken at high resolution and stitched together using the Microsoft Image Composite Editor (ICE) software, to explore a large spatial domain. Damage evolution in another specimen at approximately the same load-

[1] The compliance of the loading system has not been removed; therefore the slope of the linear region is significantly smaller than the slope of the specimen alone and the normalized displacements should not be compared directly to those determined in the simulations reported later in Sect. 4. Macroscopic scale digital image correlation (DIC) could provide adequate measurements to prescribe realistic boundary conditions arising from the loading system compliance, but this was not considered essential to the objectives of the present work.

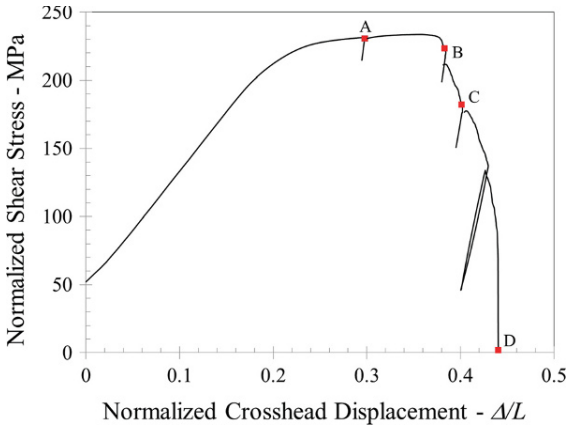

Fig. 3 Normalized shear stress (force/initial gage cross-sectional area) versus crosshead displacement (Δ) normalized by the gage length ($L = 12.22$ mm: see Fig. 2a) response of Arcan specimen. Points A and B correspond points when the specimen was unloaded and examined under an optical microscope. The point D corresponds to complete failure of the specimen. Note that the load drop near the point B is due to initiation of crack growth from the notch tips and not due to material softening

ing stages was investigated through scanning electron microscopy of the region near the notch tip. The optical microscopy focused on regions in between the two notches, while the scanning electron microscopy was restricted to the region of the notch, where very large strains are expected. These examinations eliminate polishing and etching effects and allow unhindered examination of the actual deformation and failure mechanisms; specifically, the actual strains can be determined by following the same set of grains over many deformed stages of the specimen.

2.1 Grain level measurement of local deformation

Real-time measurements of grain level deformation using digital image correlation (DIC) methods (Héripré et al. 2007; Carroll et al. 2013), X-ray tomography (Bay et al. 1999; Limodin et al. 2011), and other methods are becoming increasingly simpler to use and interpret; nevertheless, the strain levels encountered in almost all of these applications is quite small. For example, Héripré et al. (2007) examined polycrystalline plasticity and measured strains in the range of 0.1 using a square grid of gold deposited on the material; Carroll et al. (2013) used DIC to determine local strains in the vicinity of a fatigue crack; the strains measured in the vicinity of the crack were only about 0.01 even when the fatigue crack was extended. In contrast, the equivalent strains encountered in elastic-plastic fracture under monotonic loading are at least one to two orders of magnitude greater; true strains in the range of two have been estimated in some cases prior to nucleation of damage and fracture (see Fig. 1). In this range of strains, DIC typically encounters difficulties arising from image registry. Therefore, a more direct method of strain measurement is desirable. Here we develop a tracking scheme that is perhaps tedious, but still manageable; we present measurements from the interrupted tests, but in principle, this can be accomplished continuously if a loading stage attached to a microscope is used.

The principle of the method is quite simple: we follow the movement of the 2nd phase particles as a function of the global deformation and extract estimates of the local strain; it turns out that human eyes are surprisingly good in pattern recognition, and one can track the same set of particles even after substantial deformation, and sometimes, even when some of the particles break up into smaller pieces. The 2nd phase particles in the sheet are typically about 2 μm wide and about 10 μm long (see Figure 14 of Ghahremaninezhad and Ravi-Chandar 2012). A high magnification image of one such particle at Stage *B* of the loading is shown in Fig. 4; the initial orientation of the particles is such that the long direction of the particle is oriented

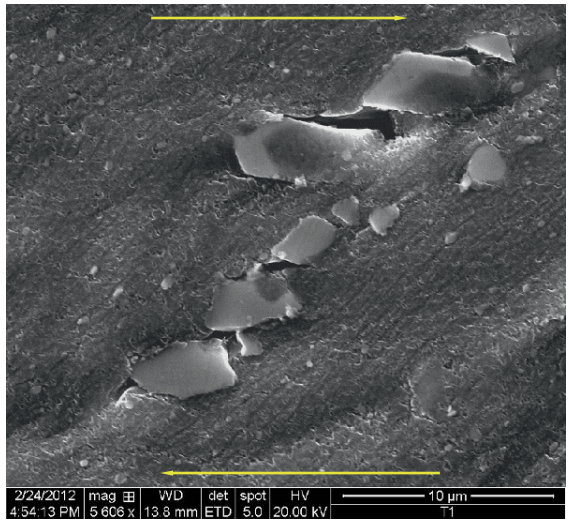

Fig. 4 SEM image of a 2nd phase particle after loading to Stage A. The long particle was initially aligned along the rolling direction (vertical), but broke into smaller fragments that rotate subsequently with the shear deformation. Note that there is no cavity formation; furthermore, the "gap" between the broken pieces is "filled" by the matrix flowing into it during the shearing deformation

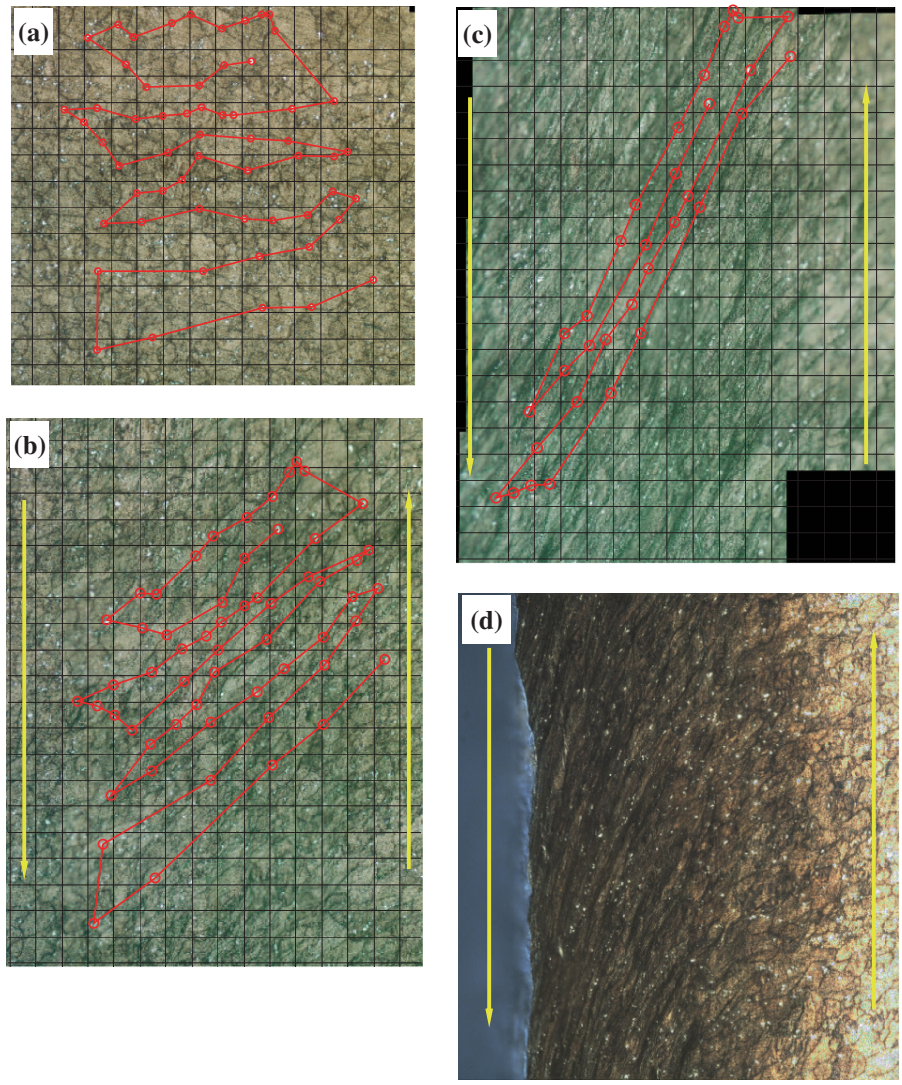

Fig. 5 Optical micrographs of the midsection of the specimen **a** undeformed, **b** Stage A, **c** Stage B and **d** Stage D. The direction of shear is indicated by the *yellow arrows*. 58 particles identified between the undeformed specimen and Stage A and 33 particles identified between Stages A and B are tracked by the *red circles* and *lines*. The image in **d** was obtained with a z-focus microscope to be able to focus on the significantly deformed specimen

with the rolling direction (vertical in this image). From the shear loading in the direction indicated by the yellow arrows, the particle rotates, and breaks into many smaller pieces. Furthermore, the pieces exhibit relative rotation with respect to each other indicating that after breaking, they continue to rotate with the deformation of the matrix. There is no indication of cavitation or other types of damage; in fact, it appears that the matrix simply "fills in" any gaps caused by the relative movement of the broken particles. Furthermore, there appears to be no failure mechanism that is generated at this scale under such shear loading; we note that failure of the specimen occurs eventually as a result of the deformation near the notch, which occurs at a triaxiality that is quite different from the pure shear state as we describe later.

Figure 5 shows four images of a region near the center of the specimen taken with an optical microscope; the grid lines superposed on the images represent squares that are 50 μm to a side. All of these images were obtained by taking multiple high resolution images at 200$\times$ magnification and stitching them together to be able to observe a much larger region. Figure 5a–d correspond to the (a) unstrained specimen, (b) loading Stage A, (c) loading Stage B, and (d) final failure. The images were then viewed under their original magnification in order to identify the same set of 2nd phase particles in each image; 58 particles were iden-

tified between the unstrained image and Stage A, and are indicated by the open red circular symbols and connecting lines in Fig. 5a, b. However, only 33 of these particles could be tracked between loading Stages A and B, mainly because the out of plane deformation of the specimen caused defocusing of some of the particles and made it difficult to identify the particles; the identified particles are indicated by the open red circular symbols and connecting lines in Fig. 5c. Finally, it was nearly impossible to identify the corresponding points between Stage B and final failure; however, if we draw tangent lines to the grain boundaries, the shear angle γ can be determined easily as indicated by the red line in Fig. 5d. This figure also indicates that the region of high shear strains is localized to an extremely narrow zone along the center of the specimen. Comparing Fig. 5a–c, it is evident that the positions of the 2nd phase particles changes significantly, but their relative order does not change, strongly suggesting that these particles are simply carried by the flow of the matrix aluminum, and therefore they represent good Lagrangian markers to evaluate the strain variation averaged over a length scale much larger than the particle size.

The deformation of the Arcan specimen can be written as $x_1 = X_1 + kX_2$, $x_2 = aX_2$, where $k = \tan\gamma$ is the amount of shear, and a is the stretch perpendicular to the direction of shear; then, the principal stretches may be estimated directly from the deformation observed in Fig. 5. These measurements indicate that the maximum principal true (logarithmic) strain (averaged over a $500 \times 500\,\mu\text{m}^2$ square) increases from 0.41 to 0.93 to 2 as we go from Stage A to Stage B to final failure. These strain levels are commensurate with the values shown in Fig. 1 for pure shear conditions. However, while the strain levels in that figure were inferred from a statistical estimate of changes in the grain dimensions, the present measurements represent a direct measurement of the strain using the *same* 2nd phase particles as Lagrangian markers. While we have only identified the average strain over a small region, the method used here clearly has the potential to resolve strains on a much smaller level, approaching grain level identification; this, however, requires that the experiments be performed in a scanning electron microscope that can image over large depth variations or in an optical microscope with a z-focus capability to reconstruct full three-dimensional image of the surface. These approaches are currently under investigation; the image in Fig. 5d was obtained using the z-focus capability of the microscope to focus over the entire field of view.

In order to explore the origins of failure under predominantly shear loading, the unstrained specimen and deformed specimens at Stages A and B, were examined in a scanning electron microscope. These observations are discussed in the next section.

2.2 Scanning electron microscopy of deformation

The development of deformation near the notch tip is rather spectacular, and is easily tracked using scanning electron microscopy. Figure 6a shows SEM images of the regions near one of the notches corresponding to the undeformed configuration. The line segment *a–b–c–d* of total length 1,400 μm identifying the edge of the specimen through the notch tip is marked by the green line in this figure for easy visual identification of the deformation. The spatial position of two additional points on the surface of the specimen near the notch (points e and f) are also marked in this figure. The deformed shape of the line *a–b–c–d* as well as the current position of the points e and f are traced through the two stages of deformation A and B in Fig. 6b, c. The specimen was initially polished to be flat and etched to reveal the grain boundaries; in the secondary electron imaging mode, the contrast in the undeformed SEM images is low. Nevertheless, some features resulting from an uneven coating of Au–Pd on the surface are visible even in the undeformed specimen, and these features are used to identify the deformation. As the deformation progresses, there is some out-of-plane deformation of the grains due to local three dimensionality of the deformation and stress fields, and this results in improved contrast in the last stage image shown in Fig. 6c. For ease of visualization of the deformation, the corresponding points in each image in Fig. 6a–c are traced by the solid and dashed lines with the arrows. We record the following important observations:

– Comparing Fig. 6a, b, the deformation of the line *a–b–c–d* is most striking; this line is seen to have "unfolded", with the segments *a–b* and *c–d* hardly exhibiting any changes, while the segment *b–c* has rotated significantly and elongated substantially. The EDM-cut notch at *c* has disappeared completely, and a "new", sharper notch has been created at the point *b*. Although we have only examined the notch at these two stages, it is apparent that as the "old"

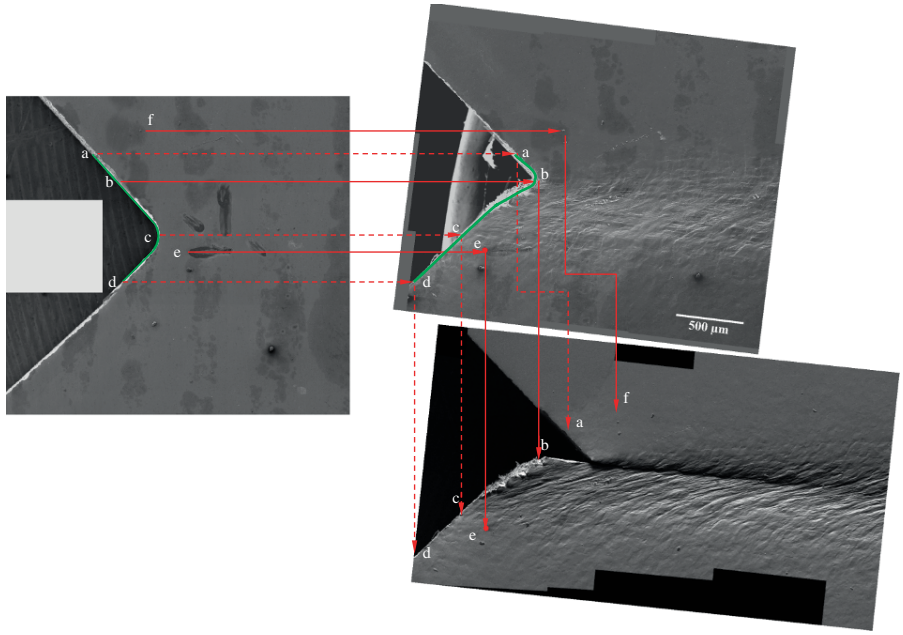

Fig. 6 SEM images of the **a** undeformed, **b** Stage A and Stage B specimens. The deformation of the notch region and selected points on the specimen is tracked between the three images. The *green line* labeled *a–b–c–d* identifies the initial notch. With deformation, it is seen that the initial notch straightens out and a new notch is formed. The contrast in **c** arises from nonuniform out-of-plane deformation of the grains. A crack is nucleated near the point *b* after significant plastic deformation

notch at *c* straightened out, the "current" notch must have moved progressively from the point *c* to the point *b*.

- It is evident that the deformation along the line *a–b–c–d* is not uniform; the deformation of each line segment can be estimated using the change in the length of each line segment. While the true logarithmic strains in segments *a–b* and *c–d* are about −0.05 and 0.13 respectively, segment *b–c* experiences rather large extensional strains, as high as 0.31.
- Segment *b–c* lies on the side of the band of high deformation extending in *x*-direction across the gage length of the specimen. This band is visualized easily in SEM images in Fig. 6c as the region of high contrast, arising from large out-of-plane-deformation at the level of the grains.
- At some loading between Fig. 6b, c, a crack was nucleated between the segment *a–b*, but very close to the point *b*, and grew towards the opposite notch region. A high-magnification image of the region near the crack in Fig 6c is shown in Fig. 7; the contrast seen in these images is from the fact that the random orientation of the grains relative to the plane of shear loading causes different out-of-plane displacements in each grain. Recalling that the rolling direction is vertical relative to the orientation of this image, it appears that there are large grain rotations, and grain elongations. Furthermore, there are many

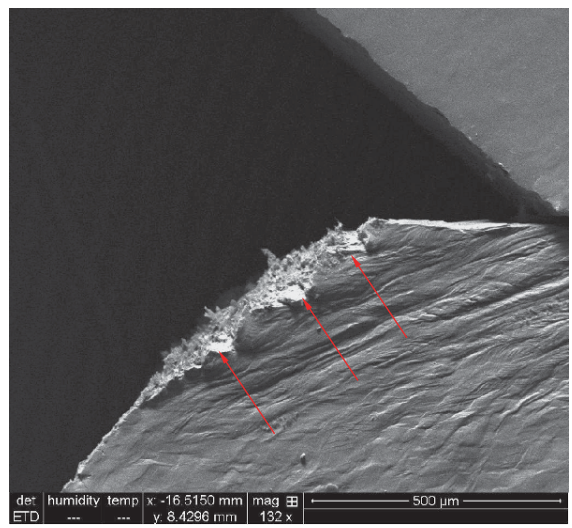

Fig. 7 A high magnification SEM image showing the crack extension from the current notch tip corresponding to the Stage *B*. The location of attempted crack nucleation at lower strain levels is marked with *arrows*. Surface relief arising from anisotropic grain deformation in the band of high deformation is easily seen in the SEM image

locations of attempted nucleation of cracks along the boundary *b–c* as identified by the red arrows in the figure.

- The crack borders on the region of highly localized shear deformation in the Arcan specimen and *does not nucleate from the original notch*. Eventually,

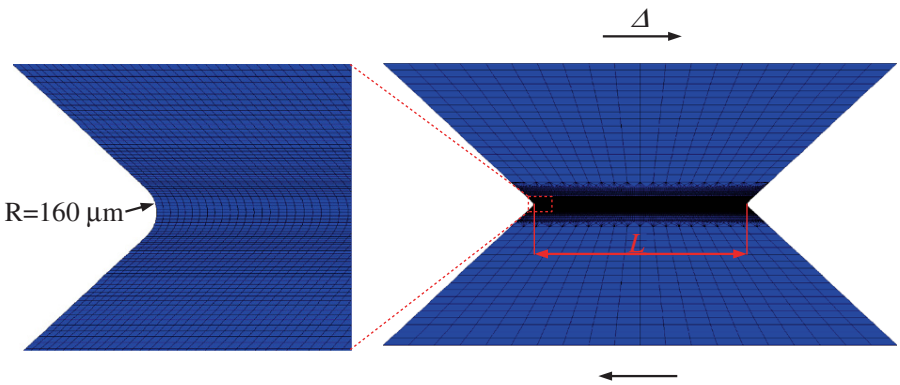

Fig. 8 **a**, **b** Schematics showing the detailed and overall mesh, respectively, used in the simulations. Fine mesh was used near the notch tip

when the crack nucleates and grows from the newly-formed notch, the material in this vicinity is quite different from the initial material in terms of its grain size, grain boundary morphology, anisotropy etc, suggesting that grain boundary morphology and texture evolution will be important aspects in dictating the onset of fracture. The stress-state is also significantly different from the initial state corresponding to the pure shear loading, as will become apparent from the numerical simulations in the next section.

These observations provide ample support to the idea that significant plastic deformation, to levels indicated by the lower bound estimate in Fig. 1, must occur prior to the onset of damage and nucleation of a crack in ductile materials such as Al 6061-T6. In the next section, we explore such crack nucleation through numerical simulations.

3 Numerical simulations

Numerical simulations of the Arcan specimen were performed in the finite element software ABAQUS/Explicit 6.11-2 with the objective of using the grain-based failure criterion of Ghahremaninezhad and Ravi-Chandar (2013) to predict the nucleation of the crack in the Arcan specimen. The geometry of the Arcan specimen was discretized using fine linear brick elements with reduced integration (C3D8R) in the gage section and gradually coarsened elements in the regions towards the outer boundaries of the specimen. The gage section consisted of 200 × 40 × 88 elements in $x \times y \times z$ directions. A mesh size of 34 × 16 × 61 μm in $x \times y \times z$ directions is used near the notch tip to explicitly represent the EDM cut notch radius, which is about 160 μm in the simulations. Since our previous studies have shown that deformation localization and failure in the polycrystalline aluminum alloy being studied here occur at a scale that is on the order of the grain size, it is expected that the finite radius of the notch will most likely influence the failure initiation in this specimen. Figure 8a, b show the detail of the fine mesh near the notch tip, and specimen geometry and overall mesh used in the simulation, respectively. The material model described in Ghahremaninezhad and Ravi-Chandar (2012, 2013) is used: specifically, the flow theory of plasticity with Hill's anisotropy is used. The Lankford parameters were measured experimentally and are given in Table 3 of Ghahremaninezhad and Ravi-Chandar (2012); the power-law hardening rule given in Eq. (2) of this article was used **only up to the Considère strain** and then extrapolated for larger strain levels through an inverse procedure where the global uniaxial response from experiments and simulations are matched (the true-stress vs strain curve is given in Figure 21b of Ghahremaninezhad and Ravi-Chandar 2012). It is recognized that an accurate prediction of material response will require the use of more complex phenomenological plasticity models where the effects of texture evolution are considered; additionally, crystal plasticity models can also provide insights into the evolution of material deformation and texture evolution in polycrystalline materials. This has been attempted recently in an effort to analyze crack tip fields in a polycrystalline material under mixed tension and shear loading (Sreeramulu et al. 2010). All these models consist of several material parameters and require lengthy material calibration programs and were not pursued in the present work.

A simple ductile failure model based on relating the strain-to-failure versus triaxiality was assumed using two calibration methods, namely, Johnson–Cook and

grain-based methods as described in detail in our previous work (Ghahremaninezhad and Ravi-Chandar 2013); these two failure criteria are shown in Fig. 1. The JC failure model is based on material parameter calibration due to Lesuer et al. (2001), which is based on strain measurements using specimen dimensions as the gage length, whereas our calibration of the grain-based failure model uses statistical measurements of strains using grain size change with respect to an intrinsic grain size as the gage length. More information on the methodology of grain based measurements is provided in (Ghahremaninezhad and Ravi-Chandar 2011, 2012, 2013). The JC failure model as implemented in ABAQUS/Explicit 6.11-2 through a cumulative damage approach is used. A linear strength degradation with a displacement to failure of $1\,\mu$m is assumed for elements at which failure initiation has been triggered, and element deletion was used to remove the elements once load carrying capacity of elements falls below 25% of that in undamaged condition; we note that while this may not be the best procedure to reach final failure, our main objective is to show that plasticity alone is responsible for much of the response of the structure and that failure processes are initiated very late, and then progress very rapidly. A semi-automatic mass scaling scheme with a minimum time increment of 10^{-6} s was used to increase the computational efficiency. Macroscopic quasi-static in-plane shear loading was simulated by specifying a constant velocity in y-direction at the top surface and zero velocity at the bottom surface. The out-of-plane displacements (z direction) at both end surfaces were fixed at zero.

A brief discussion of the length scales involved in using the failure criteria is important prior to dealing with the results of the simulations. The impetus to define strain-to-failure as a material property is driven primarily by the need to use such a parameter in numerical simulations of structural reliability. The dilemma one must face immediately is that it is essential to include a length scale in constructing such a definition; this has been considered in the literature in different ways. The most common method involves measuring the reduction in the cross-sectional area at the location of failure and using this measurement to define the strain-to-failure. This sets the scale to the characteristic transverse dimension, which is typically on the order of a few millimeters. The JC model is typically characterized at this scale. However, the model is considered a material failure model and typically reported (and commonly used) without restrictions on the size of the discretization. If we admit that they are to be used only at the scale of calibration—specimen thickness—then elements should be about a few mm large; one cannot even represent the notch in our problem with such an element size! Our simulations will demonstrate that a macroscopic failure model calibrated at the thickness scale cannot reproduce the experimentally observed behavior. A more recent method that has been used to calibrate failure models is a hybrid technique where a numerical simulation is performed to mimic the global response of the specimen and the strain at the critical element in the simulation mesh is taken to be the strain-to-failure; in this case, the failure strain is considered to be calibrated to this specific mesh size. The works of Barsoum and Faleskog (2007); Beese et al. (2010) and Dunand and Mohr (2010) fall in this category. The main drawback in this method is that it is very sensitive to the constitutive model used in the numerical simulations; as can be seen from Fig. 1 for the Al 6061, the mesh-based calibration of the failure strains does not differ too greatly from the calibration of Lesuer et al. (2001). In contrast, our calibration arises from direct measurements of the local strain on the verge of final failure, and is associated with a length scale that is of the order of a few grains.

3.1 Prediction of Johnson–Cook and grain-based failure models

The variation of the nominal stress (force/gage cross sectional area) versus normalized boundary displacement (Δ/L) obtained from the simulations using the JC and grain-based methods are shown in Fig. 9. L is the distance between the notches as shown in Fig. 8 and is used as the "gage" length. A sequence of images showing the equivalent plastic strain and triaxiality contours near the notch for the JC model calibrated by Lesuer et al. (2001) are shown in Fig. 10; these correspond to the stage B and crack initiation as marked in Fig. 9.Another sequence of images showing the equivalent plastic strain and triaxiality contours near the notch tip for the grain-based failure model is shown in Figs. 11 and 12, corresponding to stages B–C–D–E marked by diamond symbols in Fig. 9. The location of the notch tip at mid thickness of the specimen in the undeformed and deformed configurations is marked with a white square in Figs. 10a, b and 11 and by the black squares in

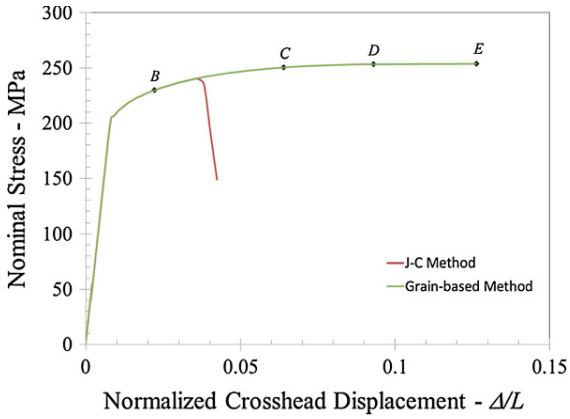

Fig. 9 Nominal Stress (force/cross sectional area) versus normalized boundary displacement (Δ/L) from simulation using grain-based and J–C methods. Points *B*–*E* denote nominal displacement levels at which the plastic strain and triaxiality are evaluated for display in Fig. 12. The point *E* corresponds to the onset of crack nucleation observed in experiments

Fig. 12 to aid in tracking deformation in the vicinity of the notch. The simulation based on the grain-based failure criterion exhibits many features that are observed in the experiments, while the JC criterion triggers failure prematurely and does not allow significant deformation near the notch region:

– It can be seen from Fig. 9 that the JC method predicts a premature failure in the specimen at a very small overall displacement in comparison to that observed in the experiments. From Fig. 10, it is seen that the notch has not deformed (or "unfolded") as observed in the experiments. The strains developed in the interior of the specimen are also significantly smaller than observed in the experiments.
– Figure 10b shows the prediction of JC method at a stage where a crack has nucleated just below the initial notch tip, and extended partially into the specimen. As can be seen from this figure, the region below the notch is where the triaxiality develops to levels of 0.5 and hence the failure strain of the JC model is reached rather early in the overall deformation. The inability of JC method to obtain a prediction of failure nucleation arises from the fact that average failure strains calibrated from measurements over a large gage length that is on the order of ten millimeters (characteristic specimen cross-sectional dimensions) is now applied

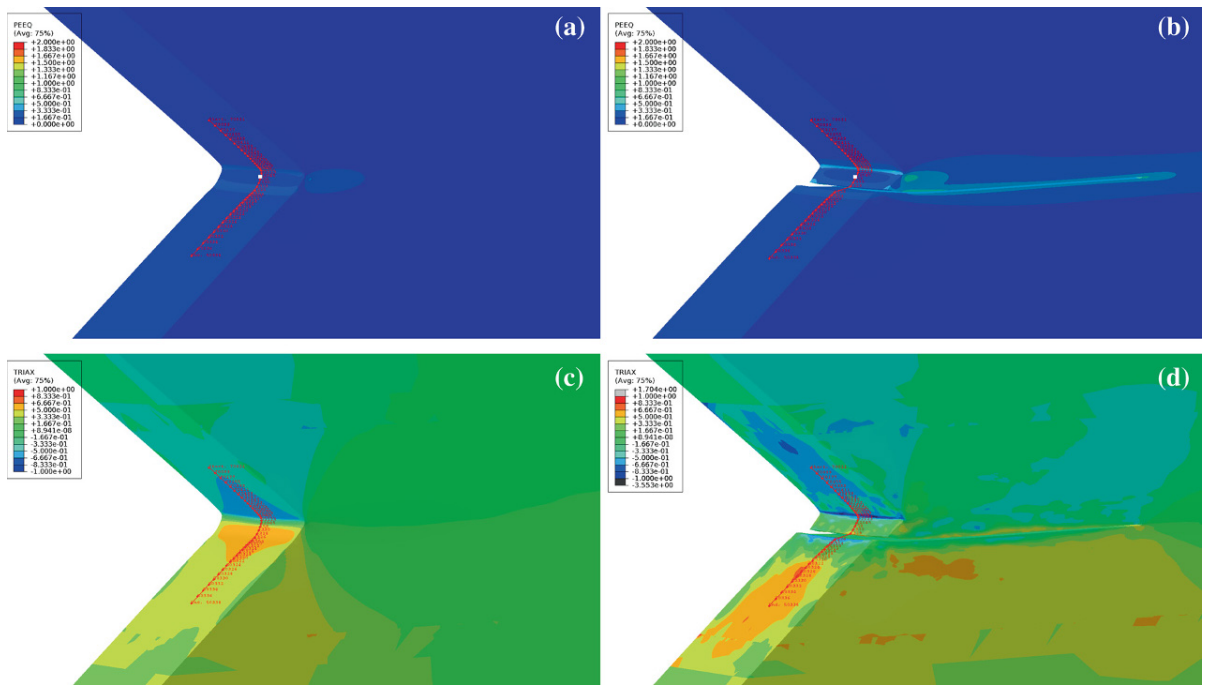

Fig. 10 **a**, **b** Plastic strain contours and deformed configurations, and **c**, **d** triaxiality contours corresponding to the stage *B* and crack initiation, respectively, as marked in Fig. 9, obtained from the JC model. The *white squares* (in **a**, **b**) indicate the location of the initial notch tip

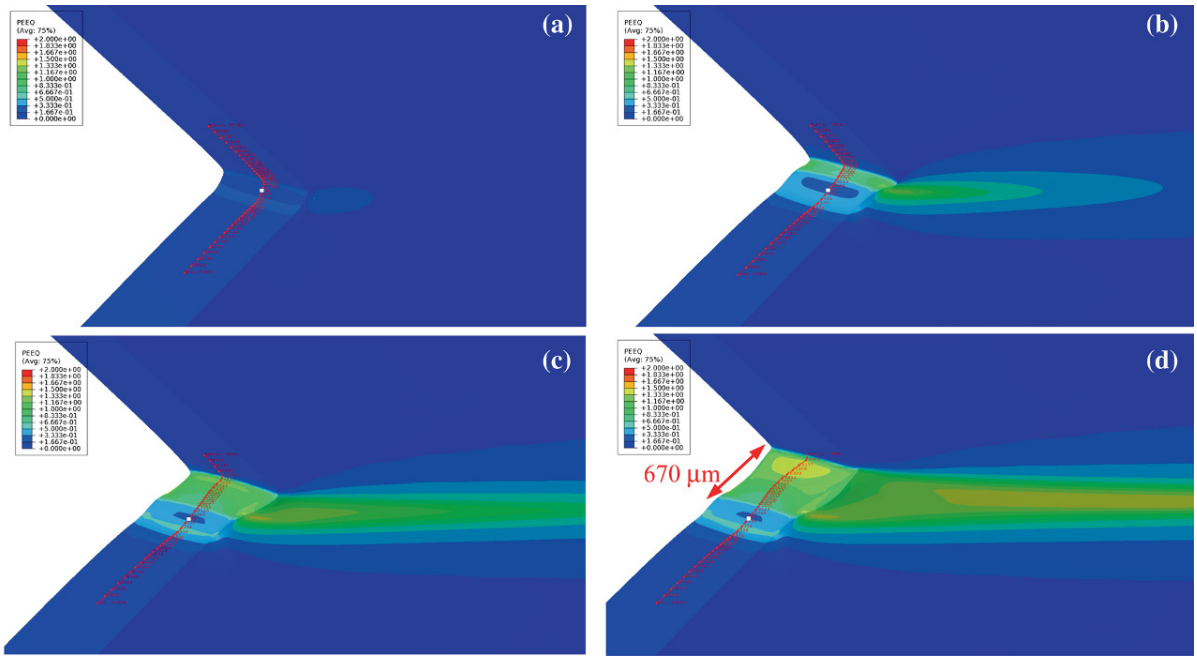

Fig. 11 **a–d** Plastic strain contours and deformed configurations at various stages of deformation (*B–E*) indicated in Fig. 9, obtained from the simulation using grain-based model. The *white squares* indicate the location of the initial notch tip

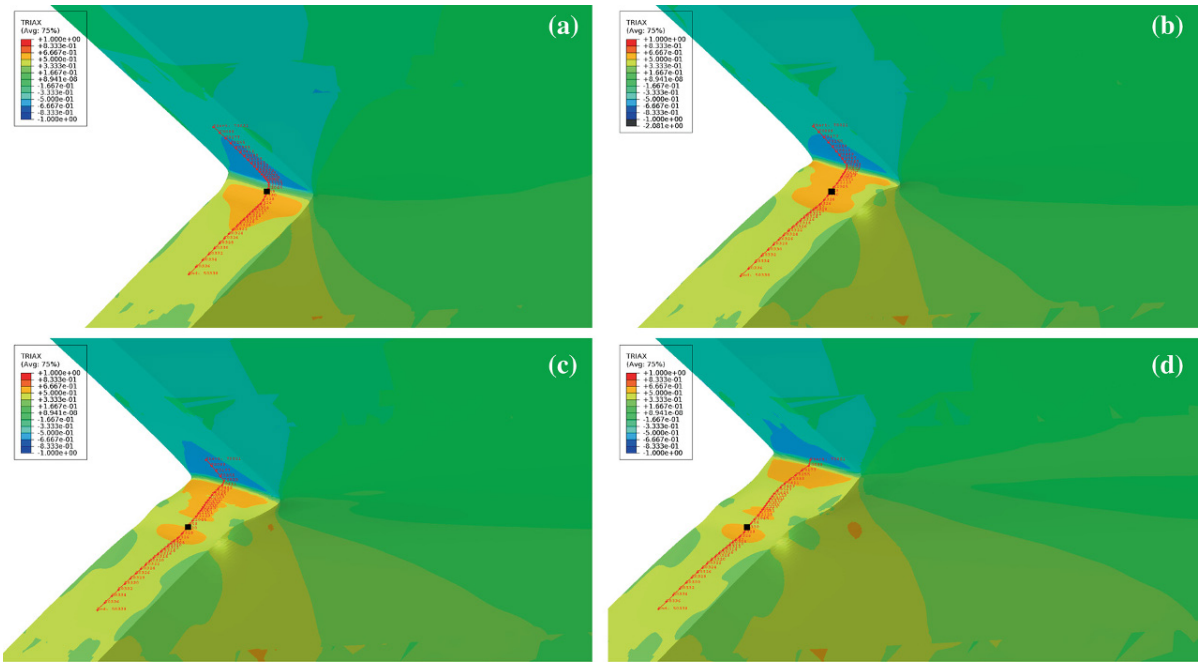

Fig. 12 **a–d** Triaxiality contours at various stages of deformation (*B–E*) as indicated in Fig. 9, obtained from the simulation using grain-based model. The *black square indicates* the initial location of the notch tip

on a scale that is a couple of orders of magnitude smaller.

– The sequence of images shown in Fig. 11 clearly indicates that the initial notch does not trigger failure when the grain-based calibration of the strain-to-failure model is used, but rather large deformation of the notch tip region occurs with the resulting "unfolding" of the notch and the development of a new notch, similar to what was observed in the experiments.
– The stage *E* in Fig. 11 corresponds to the onset of crack initiation in the experiment as determined by comparing the distance between the initial and current notch tips in the experiments; this distance was measured to be 670 μm (Line *b*–*c* in Fig. 6b). The force-displacement response from the grain-based simulation shown in Fig. 9 was terminated corresponding to the arrival of the notch at the location of crack nucleation observed in the experiment; at this point, the cumulative damage parameter was at the threshold of failure. The global response in Fig. 9 indicates a hardening behavior with no indication of macroscopic localization up to the onset of nucleation of the crack, as observed in the experiment.
– A line of length 1,850 μm drawn on the notch surface symmetrically along the middle of the thickness of the specimen as shown in Figs. 10 and 11 is used to quantify the evolution of equivalent plastic strain and stress triaxiality near the notch tip. This line is analogous to the notch line *a*–*b*–*c*–*d* that was used to identify the deformation in the experiments. First, this line also "unfolds" with overall deformation of the specimen and results in large strains of about 1.3 in the vicinity of the notch. Second, we obtain a quantitative measure of the true strain and triaxiality at points *a*, *b*, *c*, and midway between *b* and *c* (hereafter denoted as *bc*) along this line (approximating the path *d*–*c*–*b*–*a* from the experiment) during the overall deformation, and plot them in Fig. 13. It is seen from Fig. 13b that at any loading stage, the segment of the line above the current location of the notch experiences a state of compression with a triaxiality of −0.5 and the segment below the current location of the notch experiences a state of tension with a triaxiality of about 0.5. This can be readily seen from the values of triaxiality at points *a*, *c*, which lie above and below the current notch tip, respectively, during the deformation. As a point passes through the current notch tip, the stress state exhibits a rather sharp transition from compression to tension; this is demonstrated in Fig. 13b by tracking the triaxiality of the points *b* and *bc*.
– The peak plastic strain is always at the *current* notch tip; however, as the notch moves from *c* towards *b*, there is a monotonic increase in the magnitude of the peak plastic strain as the overall loading increases. Eventually, the combination of the triaxiality and plastic strain cross over the lower-bound failure envelope and crack initiation occurs. A dashed line in Fig. 13a, b marks the stage corresponding to failure as observed in the experiments. The path taken by material points at *b*, *c* and *bc* in the space of triaxiality and plastic strain is shown in Fig. 14. The triaxiality at the point *c* reaches about 0.5, but as the notch straightens out, the deformation at *c* stops at a strain level of about $\varepsilon_p = 0.3$; therefore, ductile failure is not triggered at this point. The triaxiality at the point *bc* changes rapidly as the notch approaches this

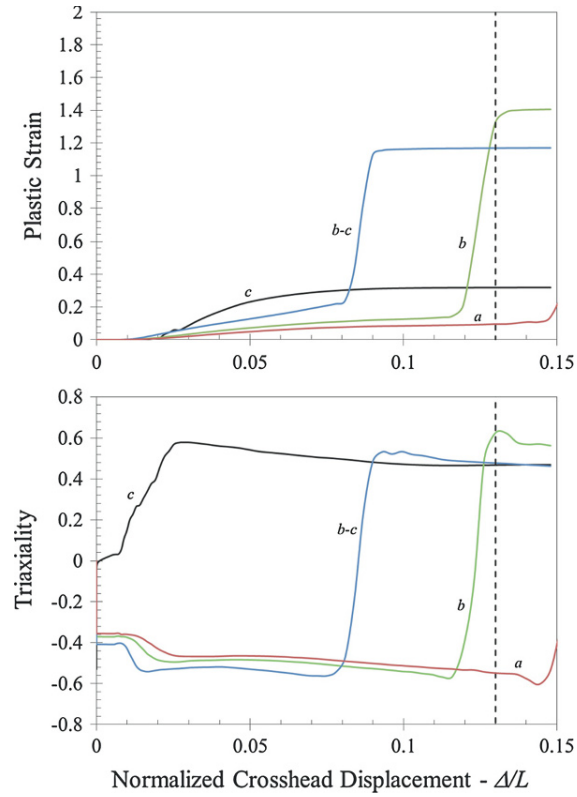

Fig. 13 Variation of (**a**) equivalent plastic strain and **b** triaxiality at points *a*, *b*, *c* and the midway point between *b* and *c* denoted by *bc* as marked in Fig. 6, obtained from the simulation using grain-based model. The dashed line marks the stage at which failure was observed in the experiments

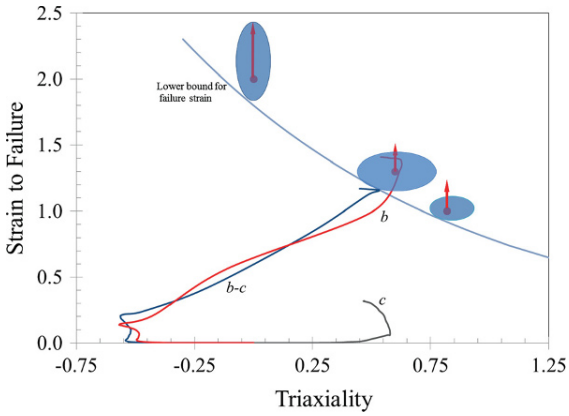

Fig. 14 The equivalent plastic strain-triaxiality variation at points *b*, *bc* and *c*, as marked in Fig. 6 superposed onto the lowerbound strain-to-failure curve obtained from grain-based measurements

point; at this stage, the plastic strain reaches about $\varepsilon_p = 1.16$; this is shown in Fig. 14 by the blue line that stops just short of penetrating the failure envelope; we note that the grain level calibration is a lower bound estimate based on statistical estimates. As the notch moves further up, the triaxiality-plastic strain state at point *b* crosses over the lower bound failure envelope and results in the crack nucleation as observed in the experiment. Therefore, even though the simulation was terminated corresponding to the arrival of the notch at the location of crack nucleation observed in the experiment, at this point, the cumulative damage parameter was at the threshold of failure, indicating that the grain-based calibration of the failure model yields an acceptable prediction of failure.

– The strains in the interior of the specimen are significantly greater than at the notch root, but they develop under a significantly lower triaxiality since these regions are under pure shear; such large strains were examined in our previous work (Ghahremaninezhad and Ravi-Chandar 2013).

The results of the numerical simulations, in comparison to the experiments indicate that the grain-based method is able to provide a realistic lower bound prediction of material deformation and failure until large strains. The primary focus here has been to elucidate a picture of material deformation and the onset of failure initiation under shear loading in ductile polycrystalline Al 6061-T6. For quantitative prediction of fracture initiation and growth, the incorporation of initial anisotropy of flow, and the further evolution of the material structure with its attendant effects on material properties is required. In particular, final fracture that appears along the reoriented microstructure needs additional considerations not included in the lower-bound failure criterion indicated in Fig. 1. While we adopted the JC method for comparison, the general outcome of this study applies to other failure models such as modified Gurson-Tvergaard-Needleman (Nahshon and Hutchinson 2008) and modified Mohr Coulomb model (Beese et al. 2010) unless these models are recalibrated with measurements on the scale of the grains; the ability of the material to deform plastically to a very large equivalent plastic strain prior to the onset of damage is an essential ingredient that must be introduced in any model.

4 Conclusions

Nucleation of a crack from a notch under dominant shear loading is considered in this article. In addition to following the load-displacement at the specimen level, optical and scanning electron microscopy are used in interrupted tests to track the deformation and failure in Al 6061-T6. The main conclusions are as follows:

– The local variation of strains can be determined to very large strain levels by proper identification and tracking of the 2nd phase particles that are distributed randomly in the material. The resolution can be improved by improving the spatial and temporal sampling during the experiments.
– The 2nd phase particles break up into smaller pieces but rotate and move with the flow of the matrix material. They do not form cavities or trigger other damage mechanisms; the matrix flows into any gaps that form as a result of differential rotation of the broken 2nd phase particles.
– The initial notch does not cause crack nucleation from its root, but triggers substantial deformation that results in the migration of the notch along the upper part of the notch; large grain deformations and rotations are observed in this vicinity. Crack nucleation occurs from the newly-formed notch, where the material is quite different from the initial material in terms of its grain size, orientation, anisotropy etc, suggesting that texture and grain boundary morphology evolution will be important aspects in dictating the onset of fracture.

– Numerical simulations using the JC model, calibrated on the basis of strains measured over length scales of specimen cross-sectional dimensions underestimate the ability of the material to strain; contradictory to experimental observations, these simulations predict premature nucleation of the crack at the root of the initial notch. It is noted that the typical calibrations of the JC model are performed at the scale of the specimen cross-section, but are always presented as material failure models, without any associated length scale.
– Numerical simulations using the grain-based calibration of Ghahremaninezhad and Ravi-Chandar (2012, 2013) are able to provide a realistic lower bound prediction of material deformation and failure until large strains. It must be emphasized that in order to use the gain-based calibration, the finite element discretization must also be at a comparable length scale—of the size of a few grains.

The lower bound failure envelope in Fig. 1 provides appropriate predictions of the plastic response of the material; for complete failure analysis, additional modeling of the changes in texture, failure properties etc is needed.

Acknowledgments This work was performed during the course of an investigation into ductile failure under two related research programs funded by the Office of Naval Research: MURI project N00014-06-1-0505-A00001 and FNC project: N00014-08-1-0189. This support is gratefully acknowledged.

References

Aoki S, Kishimoto K, Yoshida T, Sakata M, Richard HA (1990) Elastic-plastic fracture behavior of an aluminum alloy under mixed mode loading. J Phys Mech Solids 38:195–213

Bao Y, Wierzbicki T (2004) On fracture locus in the equivalent strain and stress triaxiality space. Int J Mech Sci 46:81–98

Barsoum I, Faleskog J (2007) Rupture in combined tension and shear: experiments. Int J Solids Struct 44:1768–1786

Bay BK, Smith TS, Fyhrie DP, Saad M (1999) Digital volume correlation: three-dimensional strain mapping using X-ray tomography. Exp Mech 39:217–226

Beese AM, Luo M, Li Y, Bai Y, Wierzbicki T (2010) Partially coupled anisotropic fracture model for aluminum sheets. Eng Fract Mech 77:1128–1152

Carroll JD, Abuzaid WZ, Lambros J, Sehitoglu H (2013) On the interactions between strain accumulation, microstructure and fatigue crack behavior. Int J Fract 180:223–241

Dunand M, Mohr D (2010) Hybrid experimental-numerical analysis of basic ductile fracture experiments for sheet metals. Int J Solids Struct 47:1130–1143

Ghahremaninezhad A, Ravi-Chandar K (2011) Ductile failure in polycrystalline OFHC copper. Int J Solids Struct 48:3299–3311

Ghahremaninezhad A, Ravi-Chandar K (2012) Ductile failure behavior of polycrystalline Al 6061–T6. Int J Fract 174:177–202

Ghahremaninezhad A, Ravi-Chandar K (2013) Ductile failure behavior of polycrystalline Al 6061-T6 under shear dominant loading. Int J Fract 180:23–39

Ghosal AK, Narasimhan R (1994) A finite element analysis of mixed-mode fracture initiation by ductile failure mechanisms. J Phys Mech Solids 42:953–978

Ghosal AK, Narasimhan R (1996) Numerical simulations of hole growth and ductile fracture initiation under mixed-mode loading. Int J Fract 77:281–304

Haltom SS, Kyriakides S, Ravi-Chandar K (2013) Ductile failure under combined shear and tension. Int J Solids Struct 50:1507–1522

Hancock JW, Mackenzie AC (1976) On the mechanisms of ductile failure in high-strength steels subjected to multi-axial stress-states. J Mech Phys Solids 24:147–169

Héripré E, Dexet M, Crépin J, Gélébart L, Roos A, Bornert M, Caldemaison D (2007) Coupling between experimental measurements and polycrystal finite element calculations for micromechanical study of metallic materials. Int J Plast 23:1512–1539

Hung S-C, Liechti KM (1999) Finite element analysis of the Arcan specimen for fiber reinforced composites under pure shear and biaxial loading. J Compos Mater 33:1288–1317

Johnson GR, Cook WH (1985) Fracture characteristics of three metals subject to various strains, strain rates, temperatures and pressures. Eng Fract Mech 21:31–48

Lesuer DR, Kay GJ, LeBlanc MM (2001) Modeling large strain, high-rate deformation in metals. UCRL-JC-134118, Lawrence Livermore National Laboratory

Limodin N, Rethore J, Buffiere J-Y, Hild F, Ludwig W, Rannou J, Roux S (2011) 3D X-ray microtomography volume correlation to study fatigue crack growth. Adv Eng Mater 13:186–193

Nahshon K, Hutchinson JW (2008) Modification of the Gurson model for shear. Eur J Mech A Solids 27A:1–17

Orowan E (1948) Fracture and strength of solids. Rep Prog Phys 12:185–232

Puttick KE (1960) Shear component of ductile failure. Philos Mag 5:759–762

Rice JR, Tracey DM (1969) On ductile enlargement of voids in triaxial stress fields. J Mech Phys Solids 17:201–217

Rogers HC (1960) The tensile fracture of ductile metals. Trans Metall Soc AIME 218:498–506

Sreeramulu K, Sharma P, Narasimhan R, Mishra RK (2010) Numerical simulations of crack tip fields in polycrystalline plastic solids. Eng Fract Mech 77:1253–1274

Tipper CF (1949) The fracture of metals. Metallurgia 39:133–137